Rock Mech Rock Eng (2018) 51:531–545
https://doi.org/10.1007/s00603-017-1343-7

ORIGINAL PAPER

Fracture Evolution Around a Cavity in Brittle Rock Under Uniaxial Compression and Coupled Static–Dynamic Loads

Lei Weng[1,2,3] · Xibing Li[2] · Abbas Taheri[3] · Qiuhong Wu[4] · Xiaofeng Xie[2]

Received: 11 March 2017 / Accepted: 30 September 2017 / Published online: 9 October 2017

Abstract To experimentally investigate the stability of underground excavations under high in situ stress conditions, several rock samples with a mini-tunnel were prepared and subjected to monotonic axial and coupled static–dynamic loading until failure. Mini-tunnels were generated by drilling circular or cubic cavities in the centre of granite rock blocks. Strain gauges were used to monitor the deformation of the mini-tunnels at different locations, and a high-speed camera system was used to capture the cracking and failure process. We found that the dynamic crack initiation stress, failure mode and dynamic crack velocity of the specimen all depend on the pre-stress level when the sample is under otherwise similar dynamic disturbance conditions. The crack initiation stress threshold first increased slightly and then decreased dramatically with the increase in the pre-stress value. The specimens were mainly fractured by tensile cracks parallel to the compression line under lower pre-stress, while they were severely damaged with additional shear cracks under higher pre-stress. Furthermore, the propagation velocity of the primary crack was significantly larger than that of the subsequent cracks. The effect of applying different amounts of static pre-stresses on the velocity of the primary tensile crack was similar to that observed for the crack initiation stress threshold; however, it did not affect the velocity of the secondary and subsequent tensile cracks.

Keywords Fracture process · Crack initiation stress · High-speed camera · Dynamic crack velocity · SHPB

Abbreviations

AE	Acoustic emission
DIC	Digital image correlation
ISRM	International Society for Rock Mechanics
LVDT	Linear variable deformation transducer
PFC2D	Particle flow code 2D
RFPA	Real failure process analysis
SHPB	Split Hopkinson pressure bar
UCS	Unconfined compressive strength (MPa)
UCT	Unconfined compression test
ρ	Density (kg/m^3)
n_0	Porosity
E	Young's modulus (GPa)
υ	Poisson's ratio
ν_p	Longitudinal wave velocity (m/s)
σ_t	Tensile strength (MPa)
c	Cohesion (MPa)
φ	Inner friction angle
t_s	Time-of-arrival of the specimen
t_{In}	Time-of-arrival of the incident wave
t_{TTL}	Time triggered by a TTL pulse
t_{frame}	Inter-frame time
σ_{cc}	Crack closure stress (MPa)
σ_{ci}	Crack initiation stress (MPa)
σ_{cs}	Subsequent coalescence stress (MPa)
σ_{cd}	Crack damage stress (MPa)
σ_{dci}	Dynamic crack initiation stress (MPa)
V	Velocity of crack (m/s)

✉ Lei Weng
wenglei08@gmail.com

1 School of Civil Engineering, Wuhan University, Wuhan 430072, China

2 School of Resources and Safety Engineering, Central South University, Changsha 410083, China

3 School of Civil, Environmental and Mining Engineering, The University of Adelaide, Adelaide, SA 5005, Australia

4 School of Resources and Safety Engineering, Hunan University of Science and Technology, Xiangtan 411201, China

L	Crack propagation length (mm)
t	Crack propagation time (μs)

1 Introduction

Rock engineering construction, such as for hydropower and mining engineering, usually includes cavity or tunnel excavation of rock masses in deep underground. Deep excavation may induce high stresses around the opening, which becomes the main reason for fracture or rock fall in most practical cases (Martin et al. 2003). The stability of underground openings in deep hard rock mass has long been an important problem in rock engineering. To investigate the fracturing mechanisms, pioneering studies on rock failures around openings have been performed theoretically or experimentally by several researchers (Hiramatsu and Oka 1959; Hiramatsu et al. 1962; Rummel 1971; Stephansson 1971). Their investigations show that extension cracks occur at the floor or the roof of the opening, while slabbing or spalling takes place in the side walls, depending on the experimental loading conditions. Other researchers have investigated fracture evolution around a cavity in uniaxial or biaxial compression loading conditions (Lajtai and Lajtai 1974, 1975; Gay 1976; Carter et al. 1991; Zhao et al. 2014). As shown in Fig. 1, it is generally recognised that under increasing uniaxial compression and relatively low confining stress, fractures generated around a circular opening have three types: primary tensile fracture, secondary or remote fracture and shear fracture (Lajtai and Lajtai 1975; Carter et al. 1991).

While fundamental observations of how fracture initiates, grows and interacts were obtained from experimental investigations, further understanding of the microcracking and failure process around cavity has been enhanced by numerical simulations. For instance, Fakhimi et al. (2002) used a micromechanical discontinuum program (PFC2D) to simulate the failure around a circular opening and confirmed that the results from numerical modelling are consistent with the laboratory results. Zhu et al. (2005) modelled the fracturing process and the collapse path around underground excavations with circular, elliptical and inverted U-shaped cross sections by employing an RFPA code. Wang et al. (2012) simulated the failure process around a circular opening under biaxial compression loading and found that tensile cracks dominate the failure process at low confining pressure, while shear cracks dominate the failure at higher confining pressures. Some studies (Lajtai and Lajtai 1975; Yang et al. 2015) have also focused on the fracturing behaviour of rock containing two or more cavities. Nevertheless, these experimental and numerical studies were all conducted under static or quasi-static loading conditions, disregarding dynamic loading generated by mine seismicity and blasting operations in deep underground.

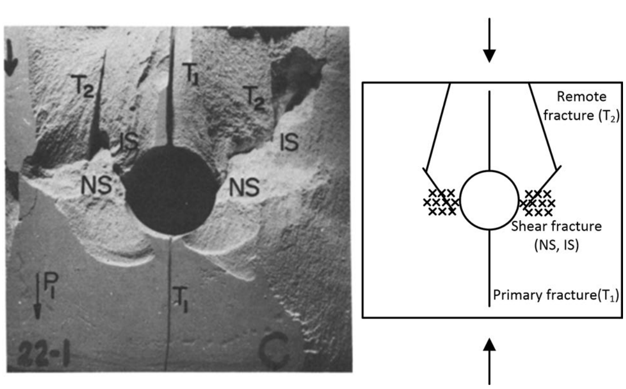

Fig. 1 Fracture development at low confining pressure (T_1: primary tensile fracture, T_2: secondary tensile fracture, *NS* normal shear fracture, *IS* inclined shear fracture) (after Lajtai and Lajtai 1975)

It is known that, under dynamic loading, high loading rate plays a significant role on the mechanical response of rocks (Frew et al. 2001; Mahmutoğlu 2006; Wang et al. 2006; Zhao 2011; Taheri et al. 2016a), as well as crack generation behaviours (Zhang et al. 1999; Zhang and Zhao 2013, 2014). Though Zou and Wong (2014) and Zou et al. (2016) studied the cracking process of flawed brittle material under dynamic loading, few works were found with respect to the characteristics of crack propagation and the failure of rock with larger pre-cut openings. In this regard, Wang et al. (2013) conducted a numerical study on the fracturing process around rock cavities under dynamic loading and found that both the compressive wave and tensile wave could influence the propagation of tensile cracks. Li et al. (2015) investigated the dynamic strength, failure mode and crack propagation characteristics of marble rock blocks with circular or elliptical holes by conducting dynamic compression tests. Some previous studies (Li et al. 2008; Zhu et al. 2012; Zhang and Zhao 2014; Li and Weng 2016) show that underground cavities under combined static stresses (or geostresses) and dynamic loading may experience excessive deformation and failure depending on the static stress level and the dynamic stress magnitude. Therefore, it is essential to investigate the fracture occurrence and growth characteristics around underground openings that are subjected to combine static and dynamic loading.

In this paper, the behaviour of differently shaped mini-tunnels being drilled into granite rock samples is investigated under unconfined compression loading. It explores the loading of the mini-tunnel samples with coupled static–dynamic loads, using a modified split Hopkinson pressure bar (SHPB) system. This paper also examines the deformation and failure process of mini-tunnels, as monitored by strain gauge measurements and a high-speed camera system. The characteristics of crack initiation stress, fracturing evolution and failure modes of the specimens with varying pre-stresses are investigated. Finally, the average crack propagation velocity is estimated from the images taken by the HS camera.

2 Experimental Set-Up

2.1 Specimen Preparation and Properties

The granite for experiments was sourced from a granite quarry in the Hunan Province of China, where a mechanical cutting method is adopted to extract rock blocks. By doing so, less damage to both the blocks and the remaining rock mass was induced when compared to the drill-and-blast method. By adopting this method, identical, intact and undisturbed rock blocks were prepared. Rock mechanics experiments widely use cylindrical specimens. In this study, however, in order to simulate the loading conditions of an underground tunnel and obtain more explicit observations of the fracture growth process, rectangular specimens were prepared and tested. In doing so, small granite blocks of $100 \times 35 \times 35$ mm^3 were cut from a large block. A high-pressure water-jet cutting technique was then used to cut a centre opening through each sample. Two shapes of opening (mini-tunnel), i.e. circular cross section with 10 mm in diameter and square cross section with 10 mm in side length, are taken into account as shown in Fig. 2. After cutting, the specimens were polished carefully to ensure smooth, flat, parallel surfaces.

The properties of the granite rock were measured by conducting standard rock mechanics laboratory tests following ISRM (International Society for Rock Mechanics) suggested methods (Bieniawski and Bernede 1979a, b). Each sample measured approximately 100 mm in height and 35 mm × 35 mm in cross section. The physical and mechanical properties of the granite specimens are tabulated in Table 1. The unconfined compressive strength (UCS) of a solid rectangular specimen is 72.66 MPa, and the ratio of UCS to tensile strength is approximately 20, which describes the granite rock as a typical brittle rock (Hajiabdolmajid et al. 2002).

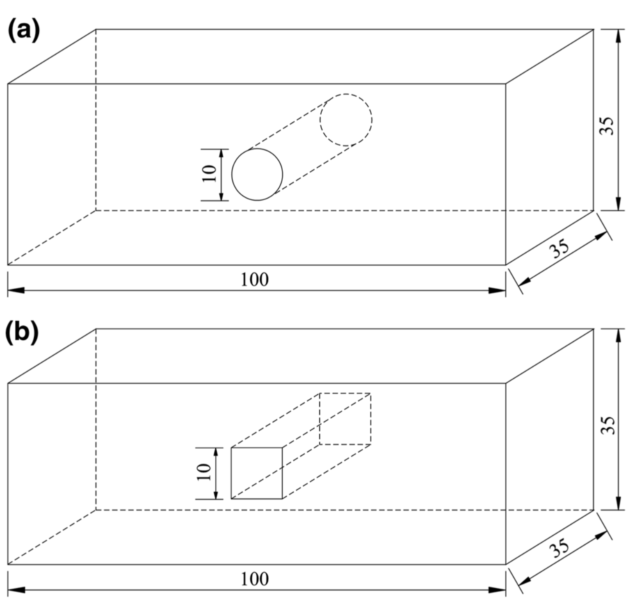

Fig. 2 Geometry of the granite specimen with **a** a circular cavity and **b** a square cavity (unit: mm)

2.2 Testing Set-Up and Method

To understand the mechanical behaviour and fracture growth of the specimens under both static compression loads and coupled static–dynamic loads, two series of tests were carried out. Those were unconfined compression test (UCT) under monotonic loading and split Hopkinson pressure bar (SHPB) tests to apply coupled static–dynamic loading to hollow samples.

2.2.1 Unconfined Compression Test

The monotonic unconfined compression test was carried out on a servo-controlled INSTRON testing system. Acoustic emission characteristics were recorded by using a PAC PCI-2 AE monitoring system. Model DH3820 strain gauges were utilised to measure the deformation behaviours of the specimens. Two strain gauges (SGs) were placed adjacent to the opening, one at roof and one at floor, and another two were positioned at the specimen ends.

2.2.2 SHPB Test

A modified SHPB system at Central South University, China, was employed to load the granite specimens with coupled static–dynamic loads. The configuration of the

Table 1 Properties of the granite specimens

Physical properties			
ρ	Density	2570	kg/m^3
n_0	Porosity	0.57	%
Elastic properties			
E	Young's modulus	35.5	GPa
υ	Poisson's ratio	0.28	–
v_p	Longitudinal wave velocity	3120-3309	m/s
Strength parameters			
σ_t	Tensile strength	4.35	MPa
UCS	Unconfined compressive strength	72.66	MPa
Mohr–Coulomb parameters			
c	Cohesion	11.70	MPa
ϕ	Internal friction angle	33.7	deg

experimental set-up is shown in Fig. 3. The SHPB system consists of stress transmission components, a striker launcher, an axial static pressure loading unit, a confining pressure loading unit (optional) and a data processing unit. Please refer to Li et al. (2008) for more detailed information about this system. Four strain gauges were mounted along the loading centre line of the specimen. Two (SG2 and SG3) were placed at the periphery of the cavity, and the other two (SG1 and SG4) were mounted at the specimen ends, to trace the strain histories during tests. This set-up is illustrated in Fig. 3.

For a typical coupled static–dynamic load test, the specimen is first loaded with an axial pre-compressive stress to a desired level. Then, the striker is launched by releasing the gas valve to generate an incident stress wave along the incident bar. The magnitude of the incident wave can be controlled by changing the gas pressure in the pressure vessel. This study mainly focuses on the fracture evolution around the opening of rock under uniaxial compression and dynamic disturbance. Therefore, the axial pre-compressive stress and the dynamic stress amplitude should be reasonably determined so that the specimen will not completely fragment or extensively fracture during the dynamic loading, but so that visible cracks are produced and thus can be captured by the HS camera. The appropriate axial pre-stress level is obtained from the unconfined compression test results, while the gas pressure for generating favourable dynamic stress amplitude is determined by trial and error.

2.2.3 HS Camera System and Synchronisation Method

A high-speed camera system was used to photograph the specimen during the dynamic loading. The system consists of a complementary metal oxide semiconductor (CMOS) sensor-based high-speed camera (PHOTRON FASTCAM SA1.1), a macrolens, a set of extension tubes and a ring-shaped flash since the HS camera can be programmed to record at higher frame rates (up to 675,000 frames/s) with a lower inter-frame time using reduced image resolution. The HS camera was set in this study to have a resolution of 192 × 192 pixel array with an inter-frame time of 10 µs (i.e. 100,000 fps). The HS camera and the oscilloscope were both triggered by a transistor–transistor logic (TTL) pulse generated by the strain gauge on the incident bar. Thus, the number of captured images until the stress wave arrived at the specimen could be obtained as follows (Zhang and Zhao 2013):

$$n = \frac{t_s - t_{In} - t_{TTL}}{t_{frame}} \quad (1)$$

where t_s is the time-of-arrival of the specimen, t_{In} is the time-of-arrival of the incident wave, t_{TTL} is the time triggered by a TTL pulse that is determined from the incident wave data and t_{frame} is the inter-frame time of the HS camera (Zhang and Zhao 2013). From Eq. (1), the recorded results out of the HS camera images and the oscilloscope data could be exactly time-matched.

3 Unconfined Compression Test Results and Analyses

Figure 4 presents the stress–strain curves with the AE count rate and accumulated AE energy variation curves. Axial stress values are obtained by readings of load cells, and the axial strain is the overall strain of the sample measured by a linear variable differential transformer (LVDT), which

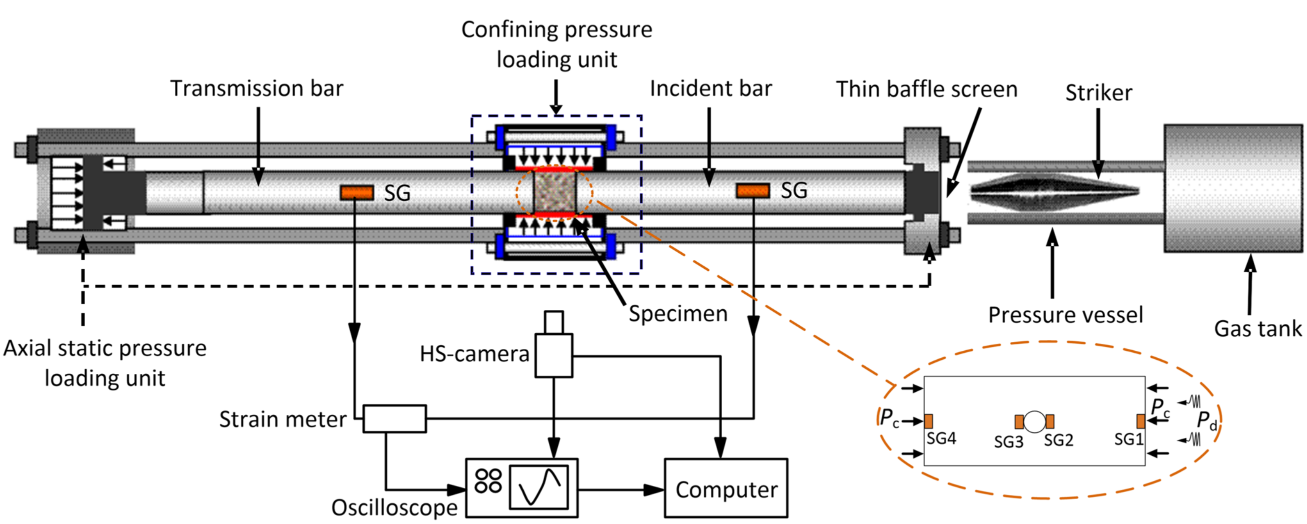

Fig. 3 Configuration of the modified SHPB system integrated with high-speed camera system

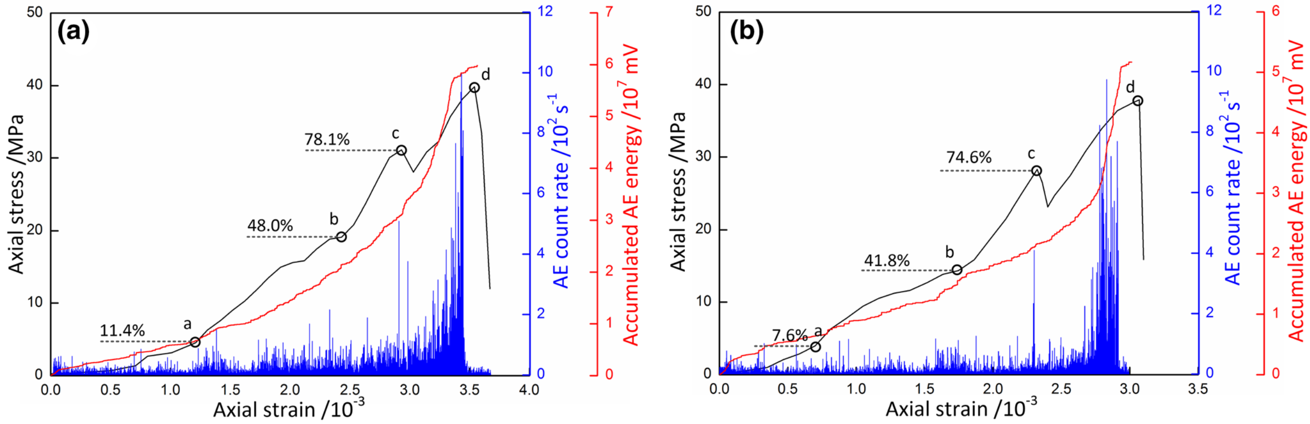

Fig. 4 Stress–strain curves associated with AE count rate and accumulated AE energy variations for **a** circular cavity specimen and **b** square cavity specimen

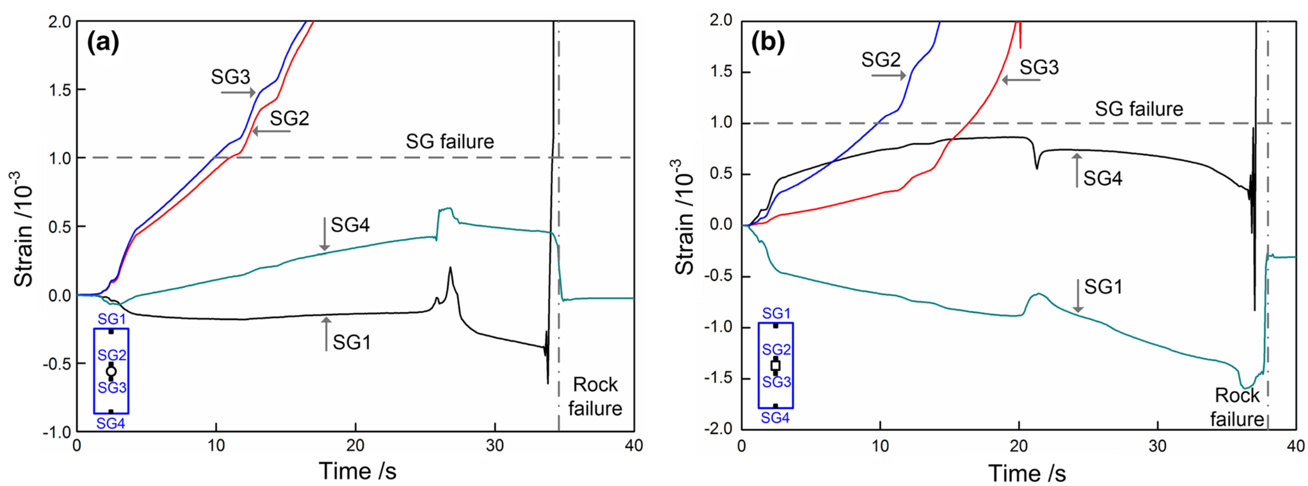

Fig. 5 Strain time history curves of the specimens **a** having a circular cavity and **b** having a square cavity

records the movement of the loading piston. We can see that the failure strengths of the circular- and square-opening specimens are lower than that of the solid specimen by 45.2 and 47.8%, respectively. Although the strengths of the two specimens are close, the peak strain of the specimen with a square opening is obviously lower than that with a circular opening. Such discrepancies may be attributed to the different local stress fields around the opening, where the stress intensity for a square opening is much higher than that for a circular one, resulting in an earlier failure under axial compressive loading.

Figure 5 shows the strain histories obtained from the strain gauges (SG1–SG4). Figure 6 demonstrates the strain gauge locations and the failure modes of the specimens. A positive value of the strain in Fig. 5 corresponds to a tensile strain, while a negative value demonstrates compression. As a typical brittle material, the specimen is supposed to

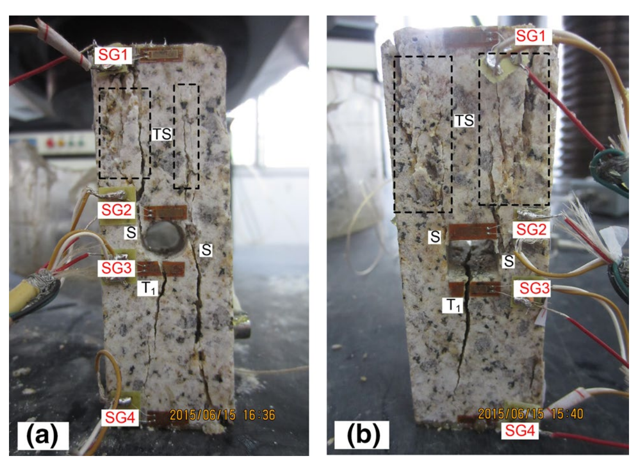

Fig. 6 Failure modes of the specimens with **a** a circular cavity and **b** a square cavity

fracture at the SG measure point when the tensile strain exceeds 1×10^{-3} (Hajiabdolmajid et al. 2002). Accordingly, the strain results in Fig. 5 indicate that failure first takes place in a tensile fashion at the periphery of the opening, while the SGs at the ends (SG1 and SG4) are damaged eventually. That damage is associated with the overall collapse of the rock sample (see Fig. 6).

To better understand the fracturing mechanism around the opening, Fig. 7 sketches the fracture growth process under monotonic uniaxial compression of a specimen that has a circular opening (Carter et al. 1991). The process is almost similar to the results shown in Fig. 6.

As shown in Fig. 4, microcracks initially tend to close at the primary loading stage (Phase oa), in which the AE events are inactive. Then, the specimen exhibits almost elastic behaviour (Phase ab). No visible fractures were observed until point b. At the beginning of phase bc, the first extension crack (primary tensile crack), marked as "T_1" in Fig. 6 (also see Fig. 7a), appears in the opening's floor when the applied load reaches about 40–50% of the peak load. It propagates further into the rock sample from the centre of the opening's floor, but slows down with the appearance of shear cracks (marked as "S" in Figs. 6 and 7b) at the side walls and the top corners. With increasing the axial load, the shear cracks, which were initiated at the compressive stress area around the opening, begin to interact with each other. They eventually merge into a longer macrofracture, causing a little drop in the stress–strain curve when the load becomes 75–80% of the peak strength (noted as "c" point in Fig. 4). As demonstrated by Taheri et al. (2016b), this point may demonstrate a crack damage stress point that is associated with the axial strain nonlinearity, or the reversal point of the total volumetric strain at the onset of dilation that is generated by crack development. It may represent the onset of unstable crack growth, which is characterised by significant structural changes to the rock. Furthermore, many more AE events were detected immediately before a drop in axial stress. This result confirms the previous statement about the crack damage stress point. Also, the accumulated AE energy curve begins to climb up sharply from the "c" point, indicating that substantial cracks generate and grow.

Simultaneously with, or just after the formation of the macroshear fracture around the opening, some more visible fractures (marked as "TS" in Figs. 6 and 7c) from far afield were observed in the specimens. These fractures, in form, are similar to the "remote fractures" observed by Carter et al. (1991). It is worth noting that the "TS" fractures form a wide fracture zone, which is mainly caused by tensile failure, although a few shear cracks were also observed. In Carter's work, however, it is suggested that the remote fractures are mainly caused by tensile failure. In the work undertaken by Carter et al. (1991), the specimen's length and height is equal to 200 mm with a 60 mm thickness; therefore, the aspect ratio is equal to 1.0. However, in the present study, following the ISRM testing standard for uniaxial compressive loading, the aspect ratio is equal to 2.86. As demonstrated by Munoz and Taheri (2017) in an experimental study using 3D digital image correlation (DIC), in specimens that have low aspect ratio values, large sections of a specimen may bear more confinement effects due to the friction between the sample and the platens. Therefore, the failure mechanism in that case is in the form of tensile failure (axial splitting failure type). However, for the specimens with a high aspect ratio, the main fracture plane is inclined with the loading direction (Li et al. 2011; Guneyli and Rusen 2016), which indicates that failure tends to be shear failure. Under such circumstances, in addition to the tensile cracks originated from the periphery of the cavity, we observe some shear failures take place at the remote area of the cavity. Therefore, prior to the whole disintegration of the specimen, the tensile cracks and

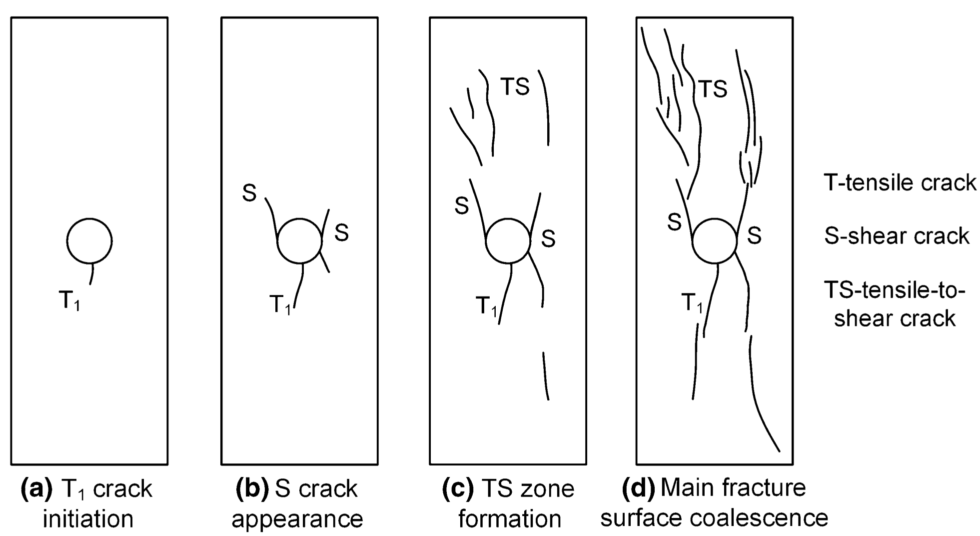

Fig. 7 Fracture evolution process of the specimen having a circular opening under monotonic compression (after Carter et al. 1991)

shear cracks form a mixed zone (labelled "TS") in the areas that are not influenced by the cavity.

With the growth of a shear crack towards the "TS" fracture zone and the "TS" fracture zone towards the loading end, the specimen finally loses its integrity. During this phase, the AE feature is extremely active.

A visual inspection of the specimens shows that the diameter of the specimen was more than 20 times bigger than the rock grain size satisfying recommendations given by the ISRM (Fairhurst and Hudson 1999). In addition, the size of the mini-tunnels was considerably larger than the grain size, and the results of tests being undertaken on different samples prepared in the same way (same sample and mini-tunnel diameter and size) follow a reasonable trend. Obviously, discontinuities may exist in the field, and then, the behaviour is not exactly similar to an intact rock being tested in the laboratory. However, in the case of very high in situ stress in an undisturbed brittle rock mass, the effect of discontinuities, if any, is not significant. As introduced by Hoek (2007) and Taheri and Tani (2008), rock strength and stiffness may decrease slightly with an increase in measurement size. Therefore, in field conditions, in the case of high in situ stress and massive rock mass, we can expect to observe almost similar results. However, the shear, primary and secondary cracks may be generated somehow at a lower in situ stress level.

4 SHPB Test Results and Analyses

To better understand how the dynamic load triggers the initiation, growth and coalescence of microcracks in the coupled static–dynamic load tests, both the static pre-stress level and dynamic load should be determined appropriately. Alternatively, it is important in this study that the fracture should not be induced by the static pre-stress but instead by the dynamic disturbance. It is known from the UCT that a visual crack will initiate when the applied axial load is about 40–50% of the UCS. Therefore, the upper level of the pre-stress is set as 20 MPa. Meanwhile, other four pre-stress levels of 15, 10, 5 and 0 MPa were applied, where 0 MPa stress denotes that the specimen is solely subjected to dynamic load.

As mentioned in Sect. 2.2.2, the magnitude of the dynamic load can be changed by adjusting the gas pressure, so that the specimen would not be severely fragmented by the dynamic load. In this study, the gas pressure for generating appropriate dynamic loads was determined to be 0.35 MPa after several trial-and-error attempts. Figure 8 shows a typical voltage signal in the incident and transmitted bars, in which the incident wave, reflected wave and transmitted wave are marked.

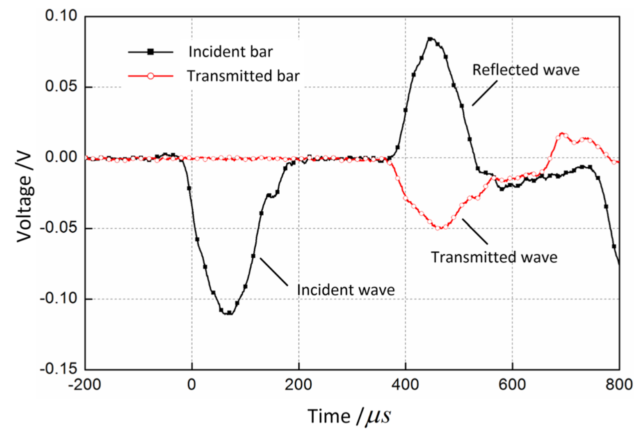

Fig. 8 Incident wave, reflected wave and transmitted wave in the bars (under 5 MPa static pre-stress and 0.35 MPa gas pressure)

4.1 Dynamic Strain Variations Around the Opening

Figure 9 presents the dynamic strain variations of specimens subjected to dynamic disturbance and pre-stresses of 5, 10 and 15 MPa. The abrupt rise of the strain magnitude indicates SG failure. It can be seen that SG2 and SG3 fail much earlier than SG1 and SG4 in all cases, indicating that cracks first initiate at the edge of the opening and then spread forward to the loading ends. Strain gauge failure is a good indicator for demonstrating crack generation time around the opening and in the specimen ends. We know that cracks are induced and propagated by tensile stress perpendicular to the loading direction because the strain values were all positive when the gauges were broken. The first tensile cracks developed under coupled static–dynamic loading were very similar to those induced under static uniaxial compression with respect to the initiation position at the early stage.

4.2 Dynamic Crack Initiation Stress

Natural rock is a heterogeneous material, containing a mass of defects such as microcracks, voids and pores. The defects inside the rock will definitely influence its macrophysical behaviour under loading. The stress–strain relation of hard brittle rock prior to failure consists of several specific deformation phases and damage thresholds, including crack closure (σ_{cc}), linear elastic deformation, crack initiation (σ_{ci}), stable crack propagation and subsequent coalescence (σ_{cs}), and crack damage (σ_{cd}) (Martin 1994, 1997; Munoz et al. 2016). The crack initiation stress σ_{ci} is a significant indicator that represents the development of the macroscopic failure process of intact rocks (Cai et al. 2004). It occurs at stress levels of 0.3–0.5 times the peak uniaxial strength (Brace et al. 1966; Holcomb and Costin 1986; Martin 1994).

However, the identified crack initiation stress of rock under different experimental conditions is not the same. For

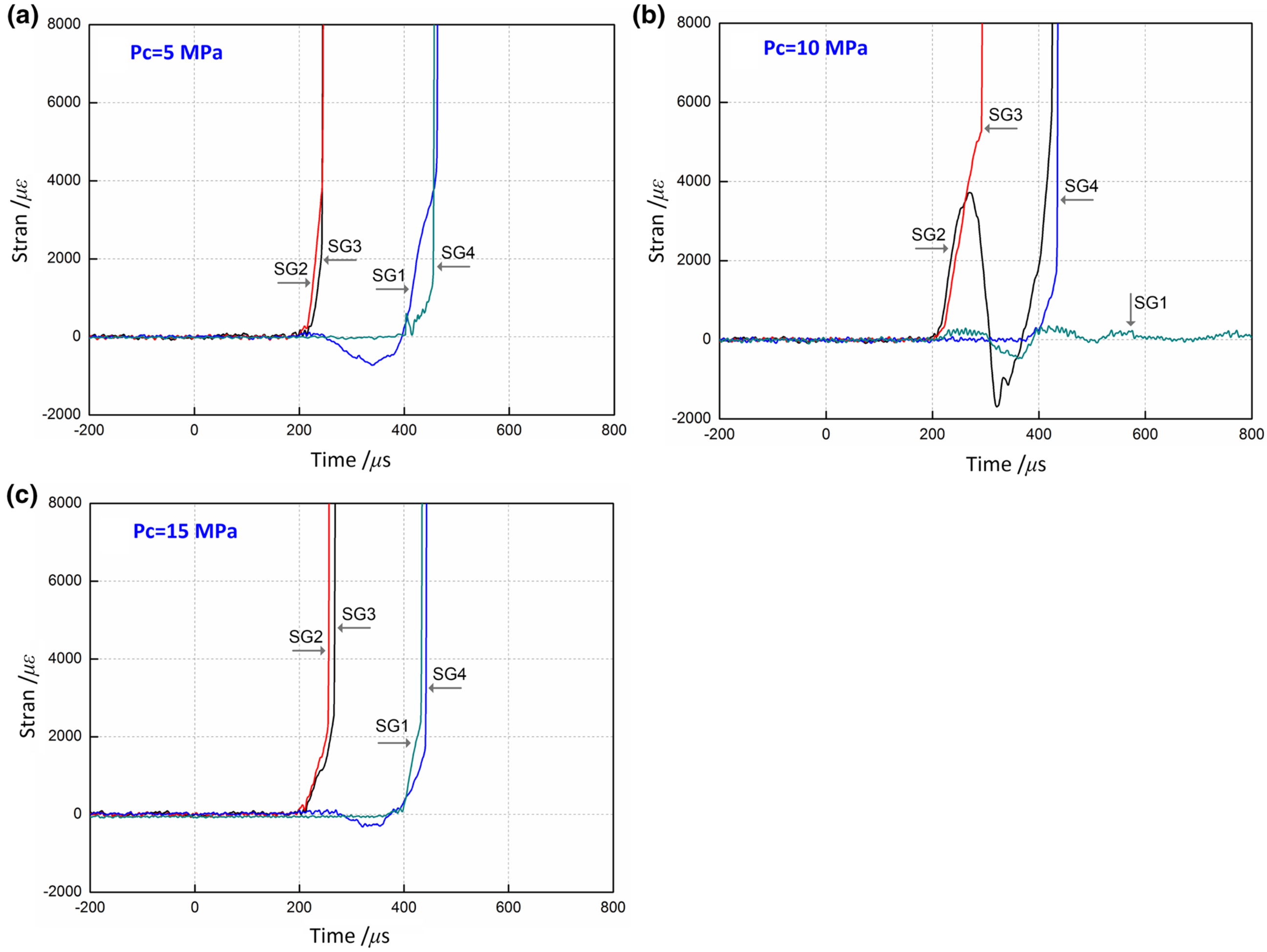

Fig. 9 Dynamic strain time histories under varying pre-stresses **a** $P_c = 5$ MPa, **b** $P_c = 10$ MPa and **c** $P_c = 15$ MPa

instance, Yang (2011) and Yang and Jing (2011) assumed that the axial stress, when first visible crack is induced, is the crack initiation stress for a pre-flawed rock specimen. Zhu et al. (2015) took the axial stress when the inner wall started caving in as the initiation stress for specimens with two circular holes. Currently, there is no standard method available to identify the crack initiation stress (σ_{dci}) of rock under dynamic loading. In this study, the value is considered to be equal to the stress level when the first tensile crack is triggered in the opening.

Figure 10 shows a typical stress history curve of specimen ci-5-1, obtained by SHPB test. In this test, σ_{dci} was determined by the following procedure. First, the stress history curve of the specimen was obtained based on stress wave theory, as shown in Fig. 10. Then, according to the synchronisation method described in Sect. 2.2.3, the HS images were exactly time-matched to the stress history curve. The starting point in the stress history curve corresponds to the time when the stress wave arrives on the right-hand end of the specimen. Finally, the dynamic crack initiation stress was

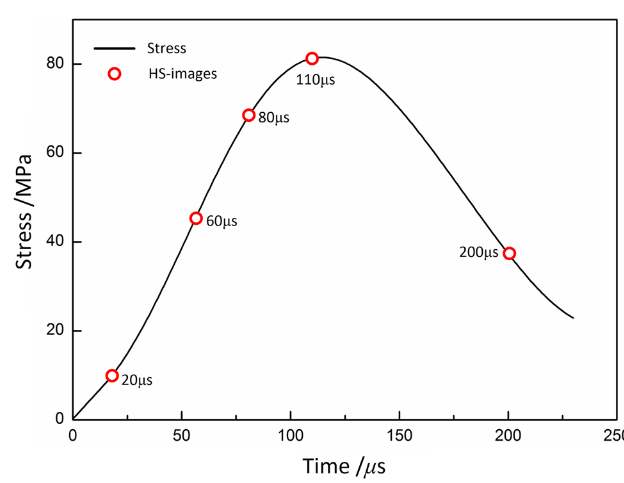

Fig. 10 Stress history curve of specimen ci-5-1

identified from the stress curve when the time-to-fracture for the first tensile crack was determined from the HS images.

Figure 11 shows that after 20 μs when the stress wave arrives at the specimen, the rock was ejected from the surrounding ground where excessive compressive stress is induced under pre-stress, yet no visible crack is generated. At 60 μs, primary tensile cracks (denoted as T_1 and T_2) were initiated from the two sides of the opening at nearly the same time. In the next 50 μs (i.e. 60–110 μs), cracks T_1 and T_2 both extended rapidly along the loading line, but the extension speed of the latter is obviously slower. At about 110 μs, the stress reached at the peak point where crack T_1 approached the left loading face, forming a coalescent crack. With multiple reflections and transmissions of the stress waves, a new tensile crack T_3 was observed at the opening at 200 μs and propagated towards the left loading face.

The first crack was observed from the HS images when the loading time reached 60 μs. Therefore, the corresponding dynamic stress at 60 μs in Fig. 10 is 45.6 MPa, equivalent to the dynamic crack initiation stress. Following this method,

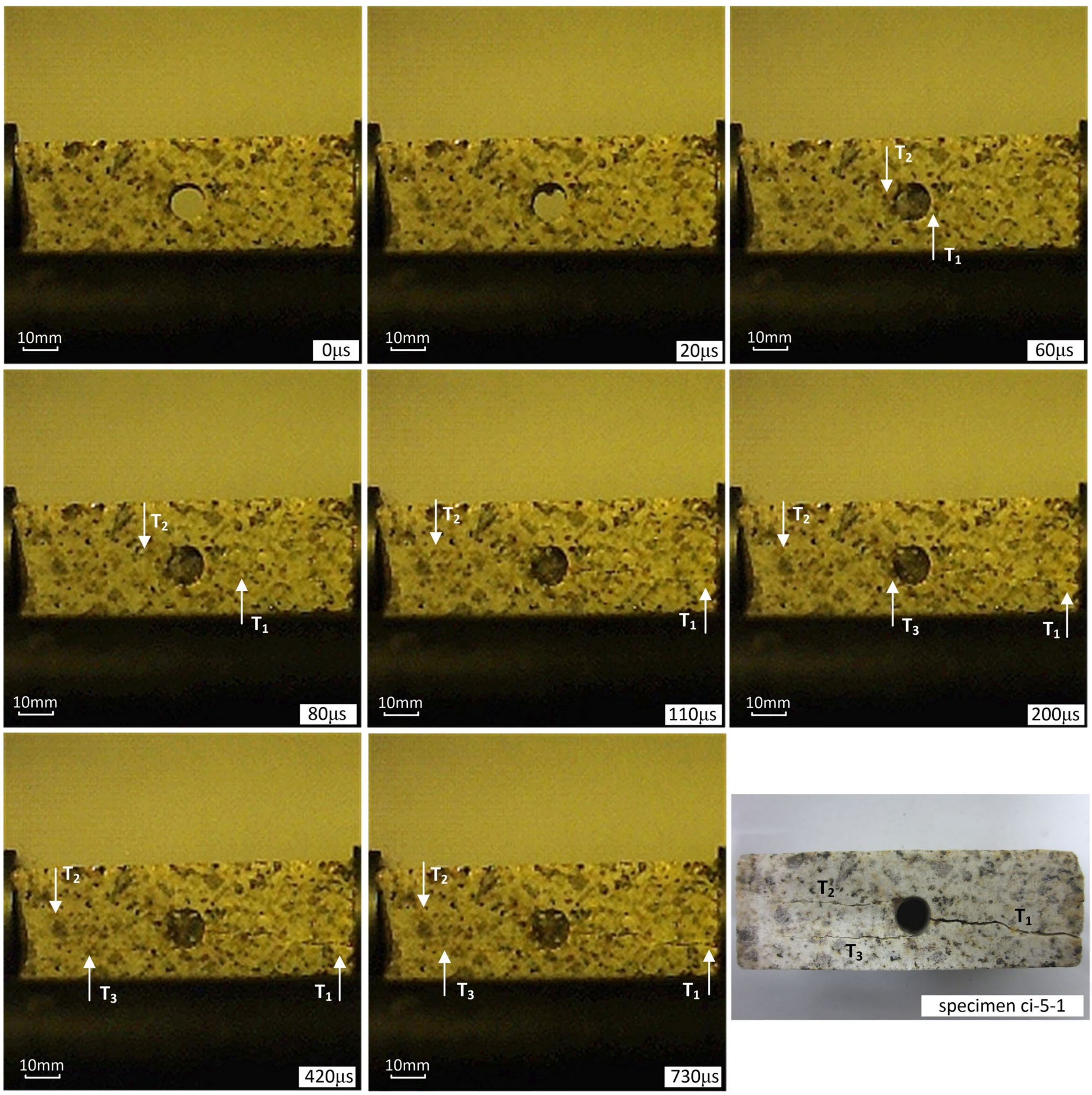

Fig. 11 Dynamic failure process of specimen ci-5-1

the dynamic crack initiation stresses σ_{dci} for the specimens under different pre-stresses were obtained; they are summarised in Fig. 12. It can be seen that the initiation stress threshold increases first and then decreases with an increase in axial pre-stressing in both the circular- and square-opening specimens. This is due to the induced stress state around the opening under static pre-stress. A low pre-stress (i.e. 5 MPa) closes the microcracks being generated due to cavity drilling; therefore, the specimen become stronger under dynamic load. As a result, higher dynamic stress is required to initiate the first crack. However, a further increase in pre-stress deforms the specimen's inelastic regime without any more recovery effects. Therefore, the specimen can be fractured earlier under dynamic loading. In this state, a lower dynamic stress can trigger and grow the crack.

The initiation stress for the circular-opening specimens was generally higher than that for square-opening specimens, indicating that the specimen with a square tunnel is more stable and therefore accommodates more dynamic crack initiation stress under what are otherwise the same pre-stress and dynamic loading conditions. This might be due to the higher stress concentration around a square opening, compared to a circular opening.

4.3 Crack Evolution Process and Failure Mode

The crack evolution process around the opening was captured by the HS camera system. Figures 13 and 14 present images of the crack propagation process at different times for the specimens with circular and square openings, respectively. The crack traces in the images are enhanced by solid arrow lines for better visualisation.

Figure 13 shows that the failure mode for the specimen with a circular opening is basically the same when the pre-stress is lower than 15 MPa. Cracks initiate from the boundary of the opening, extend towards the ends of the specimen and eventually form one or more tensile fractures parallel to the loading direction. For instance, under 10 MPa pre-stress, at 50 μs after the dynamic stress is applied on specimen ci-10-1 (see Fig. 13c), small pieces of rock are ejected out of the ground surface, where the location is known as a stress concentration region. Shortly after, tensile cracks T_1 and T_2 are generated from the cavity periphery and they spread rapidly along the loading direction towards the ends of the specimen. During the process, a tensile crack T_3 is also induced at the periphery of the opening. When the pre-stress is 20 MPa (see Fig. 13e), different types of cracks under dynamic disturbance are generated in the specimen. As shown in Fig. 13e, at first two tensile cracks T_1 and T_2 are generated, then shear crack S_1 is generated in the compressed region, and a tensile crack T_{2-1} is induced by the bifurcation of crack T_2. With the dynamic loading, the shear crack S_1 interacts with crack T_1, cutting the specimen into blocks. Crack T_{2-1} merges into crack T_2 to throw the rock slice out of the specimen. Also, a large tensile-shear fracturing zone (TS zone) is observed between the tensile cracks and the shear crack.

For the specimen with a square cavity, Fig. 14 shows that when the pre-stress is lower than 10 MPa, only tensile cracks are induced by dynamic disturbance. The crack extension direction is mainly parallel to the loading direction, which is similar to the results for specimens with circular cavities under low pre-stress. However, under higher pre-stress values, additional shear failures are observed on the specimens. For instance, the TS zone can be found on specimens sq-10-2 and sq-15-1 between the main tensile cracks (see Figs. 14c, d). Moreover, for specimen sq-20-2 under 20 MPa pre-stress, complex failure types, including tensile failure (T_1 and T_2), shear failure (S_1 and S_2) and TS zone, can be observed, breaking the specimen into several pieces.

The discussion above shows that specimens under dynamic disturbance are mainly fractured with tensile cracks parallel to the loading direction under lower axial pre-stress. While with an increase in the pre-stressing, small-scale or large-scale shear fractures can be generated. Furthermore, tensile cracks are generally incurred in or near the tensile stress concentration area, which is obviously different from the initiation point of the cracks under monotonic uniaxial compression loading. Under coupled static and dynamic loading, shear fractures can be generated and then extended in specimen. These shear cracks may interact with each other to form large-scale cracks. However, in the static unconfined compression tests, cracks are generated from the tensile stress area owing to the progressive increase in the tensile stress.

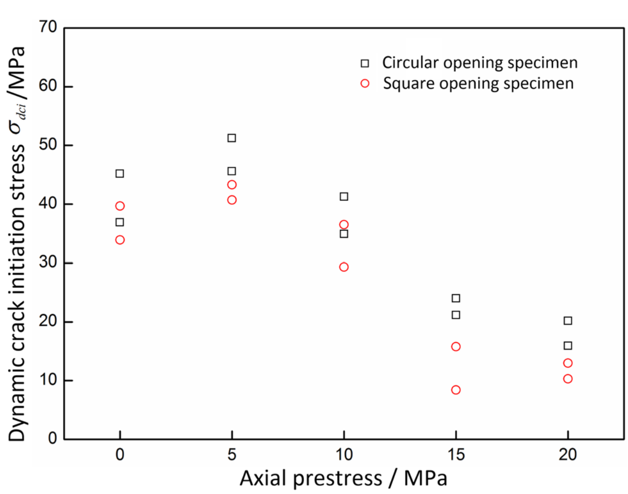

Fig. 12 Dynamic crack initiation stress of the specimens under varying pre-stresses and identical dynamic loading

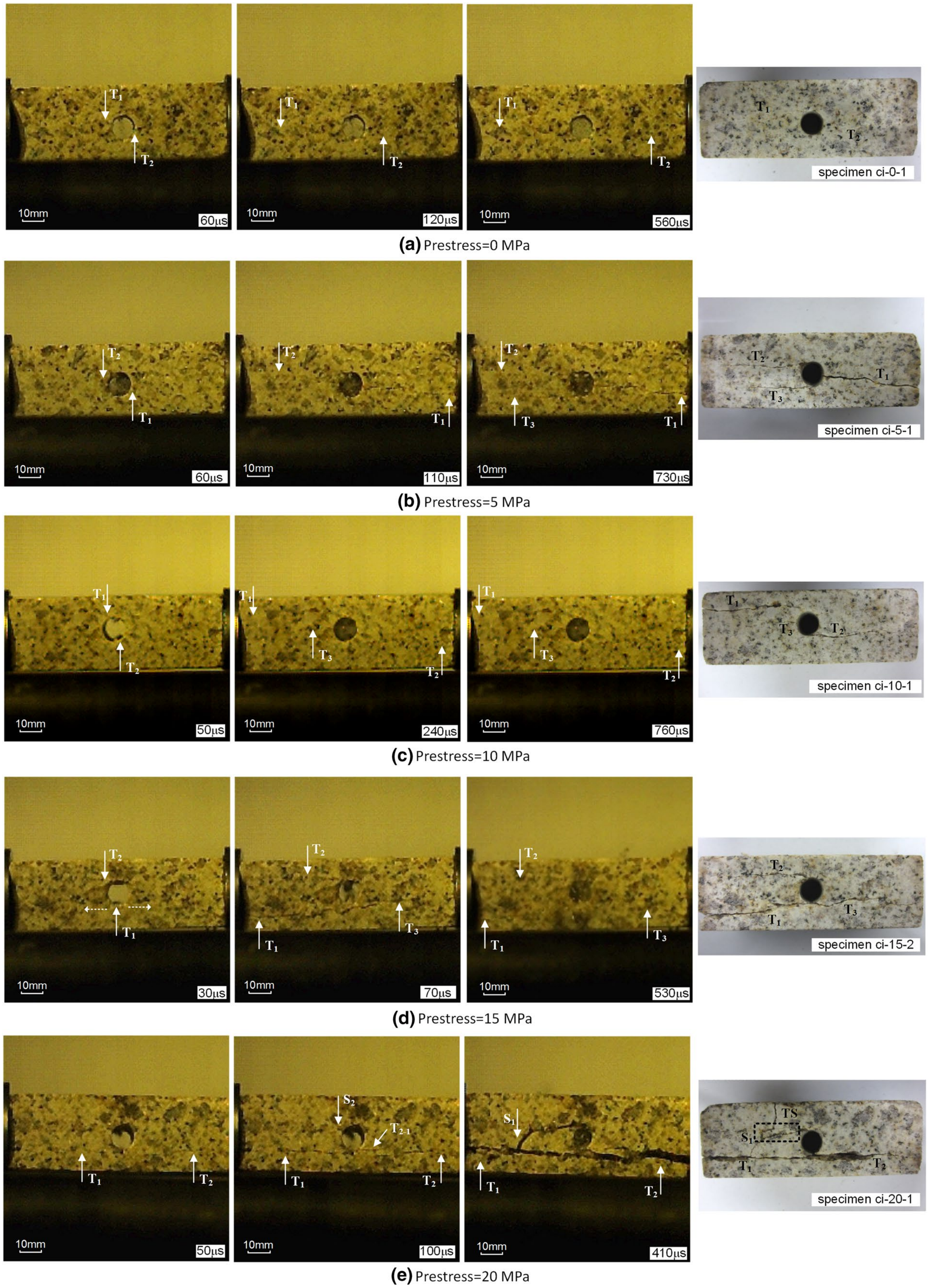

Fig. 13 Crack evolution HS images for specimens with circular cavities under varying pre-stresses

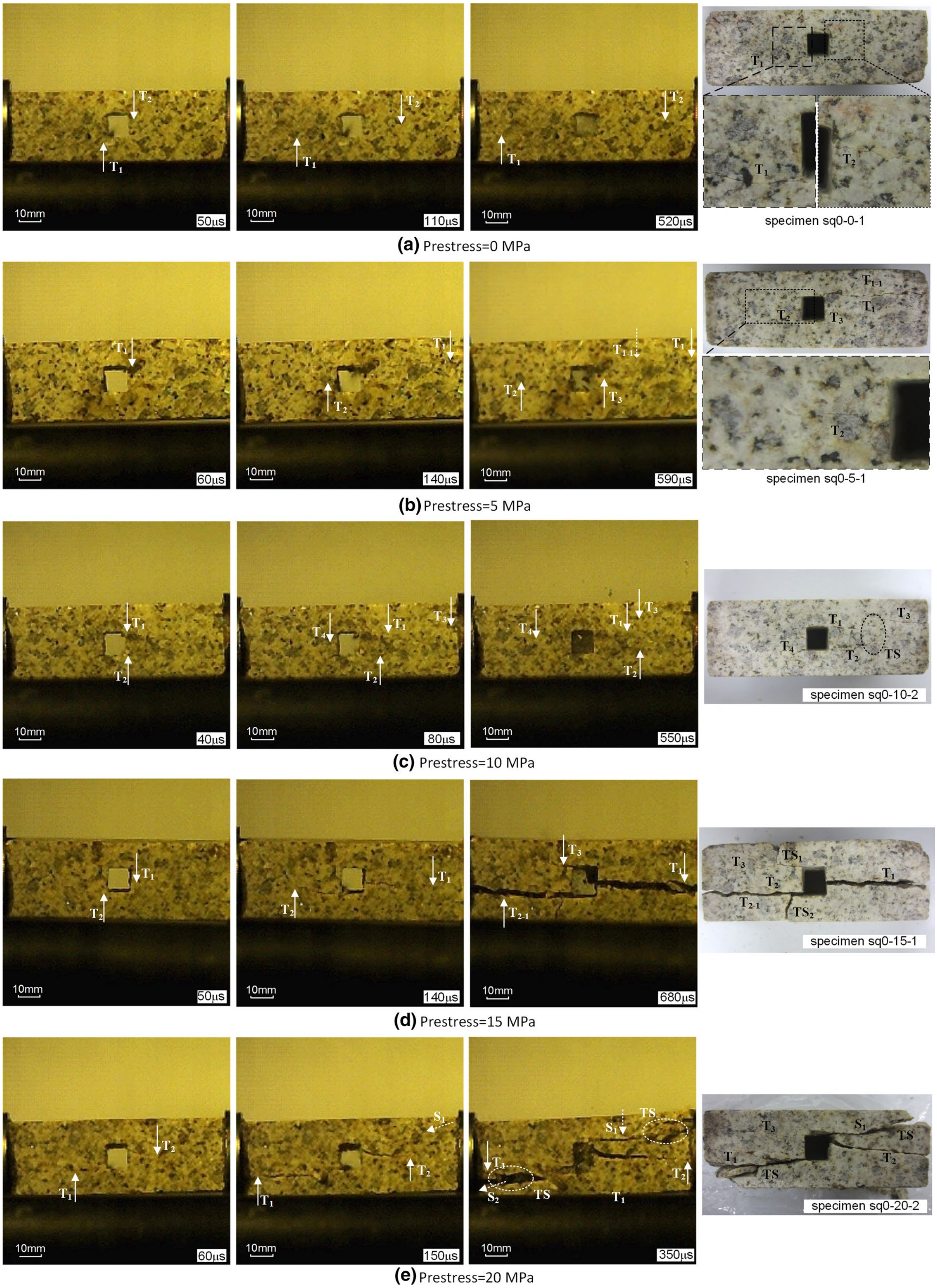

Fig. 14 Crack evolution HS images for specimens with square cavities under varying pre-stresses

4.4 Dynamic Crack Propagation Velocity

We obtained the initiation and the arrest time of the dynamic crack, as well as the propagation length, from the images taken by the HS camera. Therefore, the average crack velocity can be estimated. It is worth noting that the cracks produced by the combined static–dynamic loads are mainly tensile cracks. As the initiation and propagation of tensile cracks are easier to identify than the shear cracks, in this study, only the propagation speed of the tensile cracks was investigated. The time-to-initiation of the crack is defined as the time when the crack is generated at the boundary of the opening. The time-to-arrest is defined as the time when the crack ceases or bifurcates at the end of specimen. Considering that that there are n images between the time-to-initiation and the time-to-arrest, the total propagation time is $10n$ µs. The crack length was measured through an image processing program Photoshop CS5 by comparing the two images that represent the initiation and the arrest of the crack. The average crack propagation velocity was calculated as follows:

$$V = \frac{1000L}{10n} \tag{2}$$

where V is the average crack velocity, m/s, L is the propagation length of the crack, mm, and n is the count of the images between the time-to-initiation and time-to-arrest.

Table 2 summarises the average propagation velocity of the tensile cracks for the specimens subjected to combined static–dynamic loads. We observed that the crack speed was in the range of 63.4–681.7 m/s, which is much lower than that of common values (Zhang and Zhao 2014). A number of factors may affect the crack propagation speed, including the loading rate, the elastic energy at the crack tip and the dynamic propagation toughness (Bertram and Kalthoff 2003; Wang et al. 2016). Since the dynamic loading rate in the SHPB tests is low, the loading rate on the specimen was quite small, ranging from 21.3 to 28.9 s^{-1}. Such a low loading rate may contribute to low propagation speed of the dynamic tensile cracks.

Table 2 shows that the highest value for the velocity of the primary tensile crack (T_1) was observed when the pre-stress value was equal to 5 MPa. This velocity decreased with a further increase in the static pre-stress from 5 to 20 MPa, for both the circular- and square-opening specimens.

Table 2 Estimation of the average propagation velocity of the tensile cracks

Opening shape	Specimen	Pre-stress (MPa)	Crack label	Crack length L(mm)	Crack propagation time t (µs)	Crack velocity V (m s^{-1})
Circular opening	ci-0-1	0	T_1	28.329	70	404.7
			T_2	27.139	180	150.8
	ci-5-1	5	T_1	40.904	60	681.7
			T_2	29.162	150	194.4
			T_3	24.325	210	115.8
	ci-10-1	10	T_1	36.924	80	461.6
			T_2	32.232	190	169.6
			T_3	14.590	230	63.4
	ci-15-2	15	T_1	38.663	90	429.6
			T_2	19.689	110	179.0
			T_3	38.408	100	384.1
	ci-20-1	20	T_1	43.254	130	332.7
			T_2	36.998	180	205.5
Square opening	sq0-0-1	0	T_1	32.940	120	274.5
			T_2	31.260	130	240.5
	sq0-5-1	5	T_1	38.649	80	483.1
			T_2	23.031	180	128.0
	sq0-10-2	10	T_1	21.125	60	352.1
			T_2	20.361	150	135.7
			T_3	21.687	110	197.2
			T_4	16.174	160	101.1
	sq0-15-1	15	T_1	42.912	130	330.1
			T_2	17.147	80	214.3
			T_3	11.352	140	81.1
	sq0-20-2	20	T_1	37.141	120	309.5
			T_2	41.009	200	205.0

Meanwhile, the T_1 crack velocity of the specimen free from the pre-stress was lower than that for the specimens under pre-stress conditions. This trend is consistent with the results obtained for dynamic crack initiation stresses presented in Fig. 12. It shows that applying a small amount of pre-stress, hardens the sample and makes it more brittle, which means it can accumulate more strain energy before a tensile crack occurs under dynamic loading. Further increases in pre-stress may damage the sample under static load, and therefore, the sample will demonstrate more ductile behaviour under dynamic loading.

Table 2 shows that the velocity of subsequent tensile cracks, such as T_2, T_3 and T_4, do not show any conclusive trend with changes in pre-stress values. The velocity of the primary tensile crack is significantly greater than that of the subsequent tensile cracks. This is probably due to the stress (or energy) dissipation when the primary cracks generated in the specimen make the rock less brittle and, therefore, reduce the crack velocity of the subsequent cracks.

5 Conclusions

To investigate the failure propagation around underground openings in hard rocks under high in situ stress conditions and dynamic loading, several mini-tunnel samples were created. The samples were subjected to monotonic axial and coupled static–dynamic loading until failure. Mini-tunnels were generated by drilling circular and cubic cavities in the centre of granite rock samples. The samples were instrumented by strain gauges, and a high-speed camera was used to investigate failure behaviours in monotonic uniaxial compression and SHPB tests. This study found that:

1. Under unconfined compression, the damage of mini-tunnels was initiated with a primary tensile crack in floor area of the samples, and then, shear cracks in side walls occurred, before shear and tensile cracks were generated in other areas. However, in the SHPB tests the specimens fractured with tensile cracks parallel to the loading direction under low static pre-stress and dynamic loading. With an increase in pre-stress, additional shear cracks are gradually presented around the mini-tunnel, and violent shear failure sometimes occurs.
2. With increasing the pre-stress, the dynamic crack initiation stress threshold increases slightly at first and then decreases significantly. However, further increases in pre-stress will apply extra load on the samples, which therefore results in lower dynamic crack initiation stress. The initiation stress for circular-hole specimens was generally larger than that for square-hole samples under otherwise similar testing conditions.
3. Under dynamic induced loading, the velocity of the primary tensile crack is significantly larger than that of the subsequent cracks. The effect of static pre-stress on this velocity is similar to its effect for the dynamic crack initiation stress due to the hardening effect of small amount of pre-stress, which makes the rock behaviour more brittle. Pre-stressing does not have any significant effect on the velocity of the secondary and subsequent cracks.

Acknowledgement This research was financially supported by the National Key Research and Development Program of China (2016YFC0600706) and the National Natural Science Foundation of China (11472311 and 41272304). The first author thanks the Chinese Scholarship Council (CSC) for the financial support to the joint Ph.D. programme at the University of Adelaide, Australia. The authors would also like to acknowledge Leticia Mooney for her editorial assistance.

References

Bertram A, Kalthoff JF (2003) Crack propagation toughness of rock for the range of low to very high crack speeds. In: Key engineering materials, pp 423–430

Bieniawski ZT, Bernede MJ (1979a) Suggested methods for determining the uniaxial compressive strength and deformability of rock materials 1: Suggested method for determination of the uniaxial compressive strength of rock materials. Int J Rock Mech Min Sci 16:137–138. doi:10.1016/0148-9062(79)91450-5

Bieniawski ZT, Bernede MJ (1979b) Suggested methods for determining the uniaxial compressive strength and deformability of rock materials 2: suggested method for determination deformability of rock materials in uniaxial compression. Int J Rock Mech Min Sci 16:138–140. doi:10.1016/0148-9062(79)91451-7

Brace W, Paulding B, Scholz C (1966) Dilatancy in the fracture of crystalline rocks. J Geophys Res 71:3939–3953. doi:10.1029/JZ071i016p03939

Cai M, Kaiser PK, Tasaka Y, Maejima T, Morioka H, Minami M (2004) Generalized crack initiation and crack damage stress thresholds of brittle rock masses near underground excavations. Int J Rock Mech Min Sci 41:833–847. doi:10.1016/j.ijrmms.2004.02.001

Carter B, Lajtai E, Petukhov A (1991) Primary and remote fracture around underground cavities. Int J Numer Anal Meth Geomech 15:21–40. doi:10.1002/nag.1610150103

Fairhurst CE, Hudson JA (1999) Draft ISRM suggested method for the complete stress-strain curve for intact rock in uniaxial compression. Int J Rock Mech Min Sci 36:281–289. doi:10.1016/S0148-9062(99)00006-6

Fakhimi A, Carvalho F, Ishida T, Labuz JF (2002) Simulation of failure around a circular opening in rock. Int J Rock Mech Min Sci 39:507–515. doi:10.1016/S1365-1609(02)00041-2

Frew D, Forrestal MJ, Chen W (2001) A split Hopkinson pressure bar technique to determine compressive stress-strain data for rock materials. Exp Mech 41:40–46. doi:10.1007/BF02323102

Gay N (1976) Fracture growth around openings in large blocks of rock subjected to uniaxial and biaxial compression. Int J Rock Mech Min 13:231–243. doi:10.1016/0148-9062(76)91543-6

Guneyli H, Rusen T (2016) Effect of length-to-diameter ratio on the unconfined compressive strength of cohesive soil specimens. Bull Eng Geol Environ 75:793–806. doi:10.1007/s10064-015-0835-5

Hajiabdolmajid V, Kaiser PK, Martin CD (2002) Modelling brittle failure of rock. Int J Rock Mech Min Sci 39:731–741. doi:10.1016/S1365-1609(02)00051-5

Hiramatsu Y, Oka Y (1959) The fracture of rock around underground openings. Memoirs Faculty Engineering, Kyoto University, Japan, XXI, pt 2

Hiramatsu Y, Oka Y, Ogino S (1962) Stress around a shaft or drift excavated in ground being in a three-dimensional stress state. J Min Metall Inst Jpn 78:182–188. doi:10.2473/shigentosozai1953.78.885_182

Hoek E (2007) Practical rock engineering. In: Institution of Mining and Metallurgy, London, pp 198–200

Holcomb DJ, Costin LS (1986) Damage in brittle materials: experimental methods. Sandia National Labs., Albuquerque, NM (USA). Geomechanics Division

Lajtai E, Lajtai V (1974) The evolution of brittle fracture in rocks. J Geol Soc 130:1–16. doi:10.1144/gsjgs.130.1.0001

Lajtai E, Lajtai V (1975) The collapse of cavities. Int J Rock Mech Min 12:81–86. doi:10.1016/0148-9062(75)90001-7

Li XB, Weng L (2016) Numerical investigation on fracturing behaviors of deep-buried opening under dynamic disturbance. Tunn Undergr Sp Techol 54:61–72. doi:10.1016/j.tust.2016.01.028

Li X, Zhou Z, Lok T-S, Hong L, Yin T (2008) Innovative testing technique of rock subjected to coupled static and dynamic loads. Int J Rock Mech Min Sci 45:739–748. doi:10.1016/j.ijrmms.2007.08.013

Li DY, Li CC, Li XB (2011) Influence of sample height-to-width ratios on failure mode for rectangular prism samples of hard rock loaded in uniaxial compression. Rock Mech Rock Eng 44:253–267. doi:10.1007/s00603-010-0127-0

Li D, Cheng T, Zhou T, Li X (2015) Experimental study of the dynamic strength and fracturing characteristics of marble specimens with a single hole under impact loading. Chin J Rock Mech Eng 34:249–260

Mahmutoğlu Y (2006) The effects of strain rate and saturation on a micro-cracked marble. Eng Geol 82:137–144. doi:10.1016/j.enggeo.2005.09.001

Martin CD (1994) The strength of massive Lac du Bonnet granite around underground openings. Ph.D. Thesis, University of Manitoba

Martin CD (1997) Seventeenth Canadian geotechnical colloquium: the effect of cohesion loss and stress path on brittle rock strength. Can Geotech J 34:698–725. doi:10.1139/t97-030

Martin CD, Kaiser PK, Christiansson R (2003) Stress, instability and design of underground excavations. Int J Rock Mech Min Sci 40:1027–1047. doi:10.1016/S1365-1609(03)00110-2

Munoz H, Taheri A (2017) Specimen aspect ratio and progressive field-strain pattern development of sandstone under uniaxial compression by 3D Digital Image Correlation. J Rock Mech Geotech Eng. doi:10.1016/j.jrmge.2017.01.005

Munoz H, Taheri A, Chanda EK (2016) Pre-peak and post-peak rock strain characteristics during uniaxial compression by 3D digital image correlation. Rock Mech Rock Eng 49:2541–2554. doi:10.1007/s00603-016-0935-y

Rummel F (1971) Uniaxial compression tests on right angular rock specimens with central holes. In: Rock fracture proceeding of the international symposium on rock mechnics. Nancy, pp 90–100

Stephansson O (1971) Stability of single openings in horizontally bedded rock. Eng Geol 5:5–71. doi:10.1016/0013-7952(71)90030-5

Taheri A, Tani K (2008) Use of down-hole triaxial apparatus to estimate the mechanical properties of heterogeneous mudstone. Int J Rock Mech Min Sci 45:1390–1402. doi:10.1016/j.ijrmms.2008.01.017

Taheri A, Royle A, Yang Z, Zhao Y (2016a) Study on variations of peak strength of a sandstone during cyclic loading. Geomech Geophys Geo-Energy Geo-Resour 2:1–10. doi:10.1007/s40948-015-0017-8

Taheri A, Yfantidis N, Olivares C, Connelly B, Bastian T (2016b) Experimental study on degradation of mechanical properties of sandstone under different cyclic loadings. Geotech Test J 39:673–687. doi:10.1520/GTJ20150231

Wang QZ, Li W, Song XL (2006) A method for testing dynamic tensile strength and elastic modulus of rock materials using SHPB. Pure appl Geophys 163:1091–1100. doi:10.1007/s00024-006-0056-8

Wang SY, Sloan SW, Sheng DC, Tang CA (2012) Numerical analysis of the failure process around a circular opening in rock. Comput Geotech 39:8–16. doi:10.1016/j.compgeo.2011.08.004

Wang S, Sun L, Yang C, Yang S, Tang C (2013) Numerical study on static and dynamic fracture evolution around rock cavities. J Rock Mech Geotech Eng 5:262–276. doi:10.1016/j.jrmge.2012.10.003

Wang Q, Yang J, Zhang C, Zhou Y, Li L, Wu L, Huang R (2016) Determination of dynamic crack initiation and propagation toughness of a rock using a hybrid experimental-numerical approach. J Eng Mech ASCE 142:04016097. doi:10.1061/(ASCE)EM.1943-7889.0001155

Yang SQ (2011) Crack coalescence behavior of brittle sandstone samples containing two coplanar fissures in the process of deformation failure. Eng Fract Mech 78:3059–3081. doi:10.1016/j.engfracmech.2011.09.002

Yang SQ, Jing HW (2011) Strength failure and crack coalescence behavior of brittle sandstone samples containing a single fissure under uniaxial compression. Int J Fracture 168:227–250. doi:10.1007/s10704-010-9576-4

Yang SQ, Xu T, He L, Jing HW, Wen S, Yu QL (2015) Numerical study on failure behavior of brittle rock specimen containing pre-existing combined flaws under different confining pressure. Arch Civ Mech Eng 15:1085–1097. doi:10.1016/j.acme.2015.03.005

Zhang QB, Zhao J (2013) Effect of loading rate on fracture toughness and failure micromechanisms in marble. Eng Fract Mech 102:288–309. doi:10.1016/j.engfracmech.2013.02.009

Zhang QB, Zhao J (2014) A review of dynamic experimental techniques and mechanical behaviour of rock materials. Rock Mech Rock Eng 47:1411–1478. doi:10.1007/s00603-013-0463-y

Zhang ZX, Kou SQ, Yu J, Yu Y, Jiang LG, Lindqvist PA (1999) Effects of loading rate on rock fracture. Int J Rock Mech Min Sci 36:597–611. doi:10.1016/S0148-9062(99)00031-5

Zhao J (2011) An overview of some recent progress in rock dynamics research. Advances in rock dynamics and applications. CRC Press, Boca Raton, pp 5–33

Zhao XD, Zhang HX, Zhu WC (2014) Fracture evolution around pre-existing cylindrical cavities in brittle rocks under uniaxial compression. Trans Nonferrous Met Soc China 24:806–815. doi:10.1016/S1003-6326(14)63129-0

Zhu WC, Liu J, Tang CA, Zhao XD, Brady BH (2005) Simulation of progressive fracturing processes around underground excavations under biaxial compression. Tunn Undergr Sp Tech 20:231–247. doi:10.1016/j.tust.2004.08.008

Zhu WC, Bai Y, Li XB, Niu LL (2012) Numerical simulation on rock failure under combined static and dynamic loading during SHPB tests. Int J Impact Eng 49:142–157. doi:10.1016/j.ijimpeng.2012.04.002

Zhu TT, Jing HW, Su HJ, Yin Q, Du MR (2015) Mechanical behavior of sandstone containing double circular cavities under uniaxial compression. Chin J Geotech Eng 37:1047–1056

Zou CJ, Wong LNY (2014) Experimental studies on cracking processes and failure in marble under dynamic loading. Eng Geol 173:19–31. doi:10.1016/j.enggeo.2014.02.003

Zou CJ, Wong LNY, Loo JJ, Gan BS (2016) Different mechanical and cracking behaviors of single-flawed brittle gypsum specimens under dynamic and quasi-static loadings. Eng Geol 201:71–84. doi:10.1016/j.enggeo.2015.12.014